Arabian Journal of Chemistry (2017) **10**, 769–780

King Saud University

Arabian Journal of Chemistry

www.ksu.edu.sa
www.sciencedirect.com

ORIGINAL ARTICLE

DFT analysis and bioactivity of 2-((*E*)-(4-methoxybenzylimino)methyl)phenol and its Ni(II) and Pd(II) complexes

Amalina Mohd Tajuddin [a,*], El Hassane Anouar [b,*], Kalavathy Ramasamy [c], Bohari M. Yamin [d], Abdulrahman I. Alharthi [b], Hadariah Bahron [a]

[a] *Faculty of Applied Sciences, Universiti Teknologi MARA, 40450 Shah Alam, Selangor, Malaysia*
[b] *College of Science and Humanities, The Department of Chemistry, Prince Sattam Bin Abdulaziz University, Al-Kharj, Saudi Arabia*
[c] *Faculty of Pharmacy, Universiti Teknologi MARA, 42300, Puncak Alam, Selangor, Malaysia*
[d] *School of Chemical Sciences and Food Technology, Universiti Kebangsaan Malaysia, UKM 43600 Bangi, Selangor, Malaysia*

Received 28 August 2016; accepted 12 November 2016
Available online 18 November 2016

KEYWORDS

Schiff base;
Ni(II);
Pd(II);
HCT116;
Escherichia coli;
DFT

Abstract This paper reports the synthesis, characterisation and DFT analysis of an N,O bidentate Schiff base, ((*E*)-(4-methoxybenzylimino)methyl)phenol, (L1c) and its Ni(II) and Pd(II) complexes. The structures were elucidated via elemental analysis, UV–Visible, NMR, IR and single crystal X-ray diffraction. Complexation of L1c with Ni(II) and Pd(II) was observed to induce different degrees of bathochromic effect on $n \rightarrow \pi^*$ and $\pi \rightarrow \pi^*$ electronic transitions. A comparison of the experimental data of UV–Visible, NMR, IR and X-ray with those calculated using DFT and TD-DFT methods where five hybrid functionals were tested in gas, IEF-PCM and SS-PCM models was also carried out. The results show that the reproduction of maximum absorption bands $n \rightarrow \pi^*$ and $\pi \rightarrow \pi^*$ is strongly related to the tested hybrid functionals and solvatochromic effects. Relatively good concordance was obtained between experimental and calculated NMR chemical shifts, IR and X-ray parameters. A bioactivity evaluation against HCT116 and *Escherichia coli* displayed that the parent ligand L1c is a more superior anticancer and antibacterial agent than the positive controls of 5FU and gentamicin respectively. However, both complexes showed poor activity as anticancer agent and no activity observed against tested bacteria.

* Corresponding authors.
E-mail addresses: amalina9487@salam.uitm.edu.my (A.M. Tajuddin), anouarelhassane@yahoo.fr (E.H. Anouar).
Peer review under responsibility of King Saud University.

Production and hosting by Elsevier

1. Introduction

Although Schiff bases have been synthesised and studied extensively their continuing interest is driven by their applications in various fields and potential use in industries (Schiff, 1864). They have been reported to show antibacterial (Khan et al., 2009; Chohan et al., 2006, 2004; Kabeer et al., 2001), anticancer (Tarafder et al., 2002), antifungal (Chohan et al., 2006; Guo et al., 2007) and antileishmanial (Taha

http://dx.doi.org/10.1016/j.arabjc.2016.11.005
1878-5352

et al., 2013) activities. Phenolic Schiff bases are powerful antioxidants and free radical scavengers (Mohammed Khan et al., 2012a,b). The presence of a C═N (azomethine) functional group bearing lone electron pair of electrons in Schiff bases is responsible for their ability to adsorb onto metal surfaces, rendering them effective corrosion inhibitors for various metals such as mild steel (Abdul Ghani et al., 2014; Zainoldin et al., 2012), copper (Li et al., 1999; Ju et al., 2008), and aluminium (Negm and Zaki, 2008; Yurt et al., 2006) in acidic media (Sauri et al., 2013). In the field of coordination chemistry, Schiff bases are widely used as ligands (Mohd Tajuddin et al., 2010). Schiff bases are versatile compounds as privileged ligands, and are attractive due to their ease of synthesis. They are able to coordinate with different metals in various oxidation states to form a wide range of complexes (Ebrahimipour et al., 2014). In this regard, palladium(II) and nickel (II) Schiff base complexes have attracted much attention due to their useful applications in both chemical and biological processes (Ebrahimipour et al., 2014). Many reports have shown that these metal complexes have been used in catalysis, especially in carbon-carbon bond formation, such as Heck (Pattanayak et al., 2013), Suzuki (Cui et al., 2010) and oxidation (Ramakrishna et al., 2010) reactions. They show excellent catalytic activities in various reactions at high temperatures (> 100 °C) and in the presence of moisture (Gupta and Sutar, 2008).

Quantum chemical calculations are powerful tools to support experimental spectroscopic data such as ^{1}H and ^{13}C NMR chemical shifts (Gauss, 1992, 1993, 1995), UV–vis absorption (Bak et al., 1995; Bauernschmitt and Ahlrichs, 1996; Casida et al., 1998) and X-ray structure parameters (Mendoza-Wilson and Glossman-Mitnik, 2005; Vázquez-Vuelvas et al., 2011). In order to predict excited states, several approaches have been utilised including the TD-DFT method (Bauernschmitt and Ahlrichs, 1996; Casida et al., 1998; Furche and Ahlrichs, 2002; Quartarolo and Russo, 2011; Ramos Sousa et al., 2012; Alberto et al., 2014a,b; Mazzone et al., 2013). Numerous studies proved that the hybrid functionals B3LYP and PBE0 are appropriate to estimate the excited state energies of natural compounds (Jacquemin et al., 2007; Jacquemin et al., 2004, 2006, 2007; Woodford, 2005). We previously showed that B3P86 and B3LYP hybrid functionals were suitable to reproduce the first excited state of a series of natural polyphenols, such as flavonoids and chalcones (Anouar et al., 2012). In a recent study, Lumpi et al. used B3LYP, PBE0 and M06-2X hybrid functionals to predict the absorption and emission spectra of oligothiophene-based compounds and showed that the M06-2X hybrid functional gave more accurate results than PBE0 and B3LYP (Lumpi et al., 2013). Quartarolo and Russo applied TD-DFT (using PBE0 hybrid functional in gas and CPCM solvent models) and *ab initio* multi-Ref. coupled cluster with the resolution of identity approximation (RICC2) approaches to predict the UV/vis spectra of pyranoanthocyanins, a class of derived anthocyanin molecules; they concluded that the use of larger basis sets results in little improvement of excitation energies, and that the conformational effect has a slight influence on the λ_{MAX} predictions (*i.e.*, λ_{MAX} of the weighted Boltzmann and that of the stable conformer show similar values) (Quartarolo and Russo, 2011). In another study, the pure hybrid functionals B3LYP and PBE0, and long-range corrected hybrid functionals ωB97X and ωB97XD have been tested to predict the absorption electronic spectra of the isopentaphyrin derivative and its lutetium complex; the results showed that the reproduction of absorption bands was dependent on the absorption band types (e.g., the lowest excitation energy band for the free-base isopentaphyrin is well predicted by the ωB97XD hybrid functional) (Ramos Sousa et al., 2012).

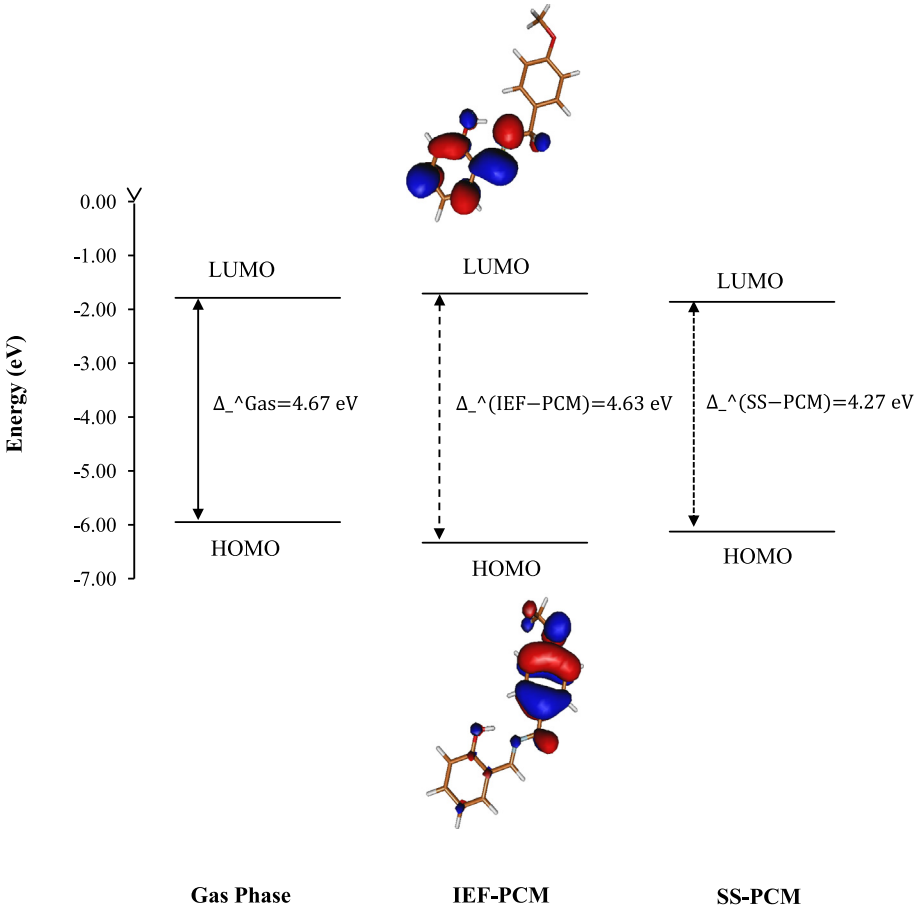

Figure 1 HOMO and LUMO energies of L1c in gas, and solvent obtained at the B3LYP level of theory.

Regarding the ^{1}H and ^{13}C NMR, the gauge-independent atomic orbital (GIAO) method is one of the most common approaches used to calculate nuclear magnetic shielding tensors (σ_{iso}) (Wolinski et al., 1990; Cheeseman et al., 1996).

In the present study, L1c phenolic Schiff base and its complexes, Ni(L1c)$_2$ and Pd(L1c)$_2$, were synthesised (Figs. 1 and 2). The current study aimed to determine complexation effect on $n \rightarrow \pi^*$ and $\pi \rightarrow \pi^*$ maximum absorption bands of L1c phenolic Schiff base by using TD-DFT hybrid functionals B3LYP, B3P86, CAM-B3LYP, M06-2X and PBE0 combined with LanL2DZ basis set in gas, and in a polarisable continuum model (PCM), for which IEF-PCM and SS-PCM formalisms are considered. In addition, the metal complexation effects were also tested on ^{1}H and ^{13}C NMR chemical shifts, IR vibrational modes and X-ray crystallographic data using the same hybrid functionals. The biological activity of L1c and its complexes was evaluated against human colorectal cancer cell line HCT116 and Gram negative bacteria *E. coli*.

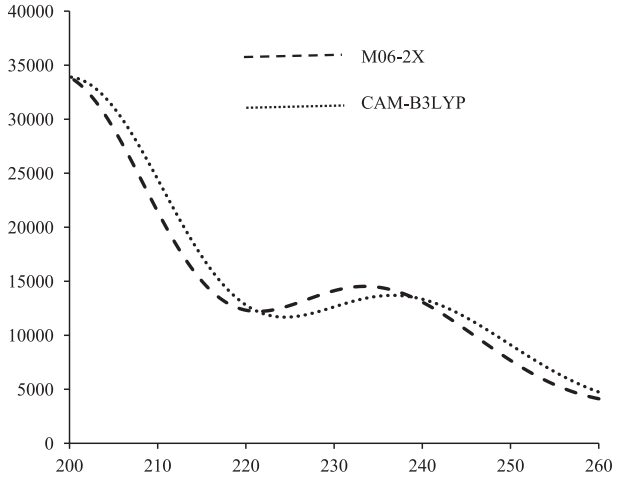

Figure 2 The predicted UV–vis spectra of L1c obtained using M06-2X and CAM-B3LYP functionals.

2. Materials and methods

All chemicals and solvents were used as purchased. Solvents were dried and freshly distilled prior to usage. Microanalyses for C, H and N were determined using a Thermo Finnigan Flash Elemental Analyzer 2000. Melting points were determined in evacuated capillaries using Buchii-B454 and were not corrected. ^{1}H and ^{13}C NMR spectra were recorded on a Bruker Varian spectrometer (300 MHz) in deuterated $CDCl_3$. Chemical shifts (δ) were reported in ppm relative to Si$(CH_3)_4$, using the residual solvent resonances as internal references. The UV–vis spectra were obtained in chloroform in the 200–900 nm range using Perkin Elmer UV–vis Lambda 35 spectrophotometer at room temperature. The infrared spectra (IR) in KBr pellets were recorded using a Perkin Elmer Spectrum GX spectrophotometer (Perkin Elmer, Waltham, MA, USA) in the range of 400–4000 cm^{-1}. Single crystal X-ray experiments were performed on Bruker D-QUEST diffractometer (Bruker, AXS Inc., Madison, WI, USA) using graphite-monochromated Mo-Kα radiation (λ = 0.71073 Å).

2.1. Synthesis of Schiff base L1c

An ethanolic solution of salicylaldehyde (40 mmol, 4.8897 g) was added dropwise into 4-methoxybenzylamine (40 mmol, 5.6979 g) in 10 mL ethanol in a round-bottomed flask to give a bright yellow solution. The mixture was stirred for 15 min (Scheme 1). The mixture was left in an ice bath upon which a yellow semicrystalline solid appeared. The solid was filtered off, washed with ice-cold ethanol and air-dried at room temperature. The resulted product was identified as 2-((*E*)-(4-methoxybenzylimino)methyl)phenol, a phenolic Schiff base named L1c. Yellow solid; yield, 68%; m.p. 62–65 °C. Anal. Calcd. for $C_{15}H_{15}NO_2$ (241.29 g mol^{-1}): C, 74.67; H, 6.27; N, 5.80; Found: C, 74.77; H, 6.28; N, 5.97. IR (KBr, cm^{-1}): 3457 (OH), 2935 (C—H stretch), 1630 (C=N), 1326 (C—N), 1248

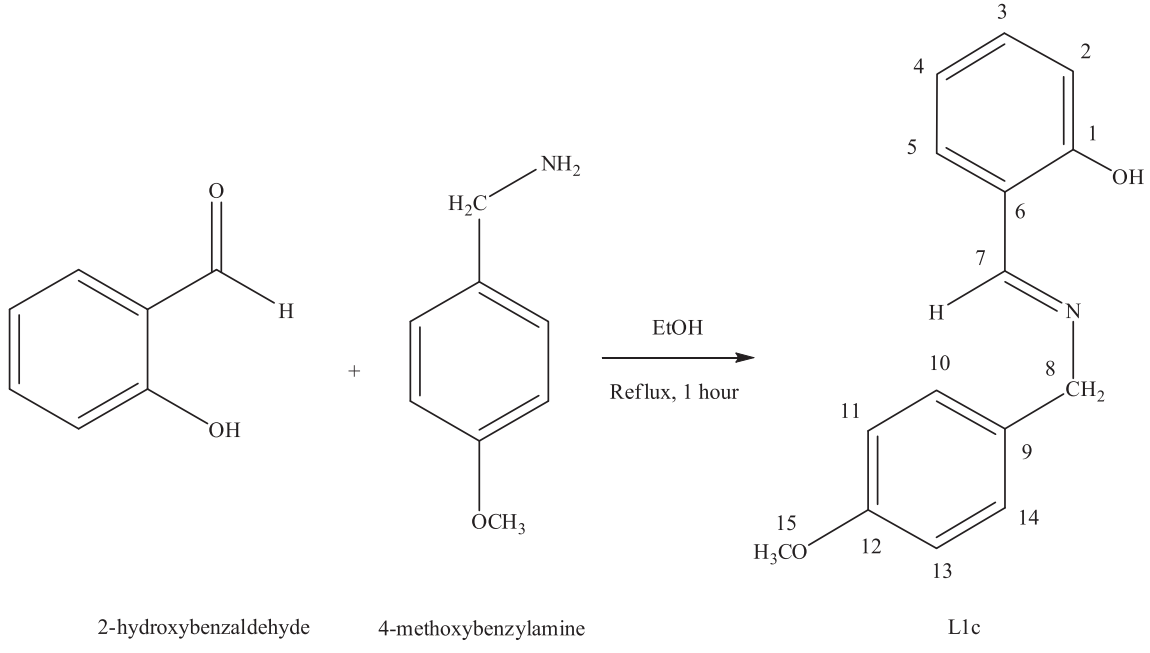

Scheme 1 Synthesis of phenolic Schiff base L1c.

(C—O). UV–vis ($CHCl_3$) λ_{max} (ε, $M^{-1}\,cm^{-1}$) = 258 (8500), 287 (11,250). ^1H and ^{13}C NMR (300 MHz, $CDCl_3$) are presented in Table 1 and Table 1S in Supplementary Materials.

2.2. Synthesis of $Pd(L1c)_2$ and $Ni(L1c)_2$ complexes

$Pd(OAc)_2$ (2.5 mmol, 0.5618 g) in 10 mL of MeCN was added to a solution of L1c (5 mmol, 1.2074 g) in 10 mL of MeCN (Scheme 2). The resulting mixture was then stirred and refluxed for 4 h upon which a turmeric yellow solid was formed. The solid formed was filtered off, washed with ice-cold MeCN and air-dried at room temperature. The solid product was recrystallised from chloroform yielding yellow crystal. Turmeric yellow solid; yield, 91%; m.p. 230–238 °C. Anal. Calcd. for $C_{30}H_{28}N_2O_4Pd$ (586.97 g mol^{-1}): C, 61.39; H, 4.81; N, 4.77; Found: C, 61.63; H, 3.67; N, 4.71. IR (KBr, cm^{-1}): 2926 (C—H stretch), 1606 (C═N), 1342 (C—N), 1318 (C—O), 596 (Pd—N), 434 (Pd—O). UV–vis ($CHCl_3$) λ_{max} (ε, $M^{-1}\,cm^{-1}$) = 285 (23,750), 399 (3000). ^1H and ^{13}C NMR (300 MHz, $CDCl_3$) are presented in Table 2 and Table 2S.

In a similar procedure, nickel(II) acetate tetrahydrate, $Ni(OAc)_2{\cdot}4H_2O$ (2.5 mmol, 0.6216 g) was used, which resulted in the formation of $Ni(L1c)_2$ complex as a green solid. X-ray quality green single crystals were obtained by slow evaporation in chloroform at room temperature. Green solid; yield, 43%; m.p. 196–199 °C. Anal. Calcd. for $C_{30}H_{28}N_2O_4Ni$ (539.25 g mol^{-1}): C, 66.82; H, 5.23; N, 5.19; Found: C, 67.03; H, 5.28; N, 5.15. IR (KBr, cm^{-1}): 2925 (C—H stretch), 1605 (C═N), 1391 (C—N), 1325 (C—O), 598 (Ni—N), 437 (Ni—O). UV–vis ($CHCl_3$) λ_{max} (ε, $M^{-1}\,cm^{-1}$) = 297 (5000), 389 (2500).

2.3. Computational methods

Ground-state geometry optimisation of L1c phenolic Schiff base, $Ni(L1c)_2$ and $Pd(L1c)_2$ complexes was carried out using five different hybrid functionals B3LYP, B3P86, CAM-B3LYP, M06-2X and PBE0 combined with LanL2DZ basis set (Becke, 1993). The frequency analyses were performed at the same level of theory. The ground state minima were confirmed by the absence of imaginary frequencies. The vibrational modes were calculated at the same level of theory and scaled by a factor of 0.9679 (Andersson and Uvdal, 2005).

Excited singlet state (ES) energies were calculated using TD-DFT method. The maximum absorption bands, vertical electronic excitations and oscillator strengths ($f > 0$ for allowed transition) were calculated (Furche and Ahlrichs, 2002; Scalmani et al., 2006). The predicted ^1H and ^{13}C NMR magnetic isotropic shielding tensors (σ) were calculated using the standard Gauge-Independent Atomic Orbital (GIAO) approach (Gauss, 1993), using the aforementioned hybrid functionals. The isotropic shielding values were used to calculate the isotropic chemical shifts δ with respect to tetramethylsilane ($Si(CH_3)_4$). $\delta_{iso}(X) = \sigma_{TMS}(X) - \sigma_{iso}(X)$, where δ_{iso} is isotropic chemical shift and σ_{iso} isotropic shielding constant.

Table 1 Predicted and experimental ^1H and ^{13}C chemical shifts of L1c calculated at different levels and phases.

	B3LYP		B3P86		CAM-B3LYP		M06-2X		PBE0		Exp.
	Gas	IEF-PCM	Gas	IEF-PCM	Gas	IEF-PCM	Gas	IEF-PCM	Gas	IEF-PCM	
^1H NMR											
H1	13.6	13.7	13.9	13.9	13.6	13.5	13.3	13.4	13.7	13.8	13.5
H2	7.3	7.1	7.1	7.1	7.3	6.9	7.4	7.3	7.2	7.1	6.9
H3	7.3	7.3	7.2	7.2	7.3	7.3	7.4	7.4	7.2	7.3	7.3
H4	6.9	7.0	6.8	6.9	6.9	7.3	7.0	7.1	6.9	6.9	7.3
H5	7.0	7.2	7.0	7.1	7.1	7.3	7.2	7.3	7.0	7.1	7.3
H7	8.3	8.3	7.9	8.0	8.2	8.4	8.4	8.4	8.1	8.1	8.4
H8	4.9	5.0	5.2	5.2	4.8	4.8	4.6	4.8	5.0	5.1	4.8
H10	7.0	7.1	6.9	7.0	7.0	7.3	7.1	7.2	7.0	7.1	7.3
H11	7.2	7.0	7.1	7.0	7.2	6.9	7.3	7.1	7.1	7.0	6.9
H13	6.6	6.7	6.6	6.7	6.6	6.9	6.7	6.8	6.6	6.7	6.9
H14	7.5	7.3	7.4	7.3	7.5	7.3	7.6	7.4	7.5	7.3	7.3
H15	4.1	4.0	4.5	4.3	4.2	3.8	3.7	3.6	4.2	4.1	3.8
^{13}C NMR											
C1	163	160	163	162	161	160	150	156	159	161	165
C2	119	116	119	118	119	118	113	120	114	118	117
C3	131	129	132	132	132	132	125	133	128	132	132
C4	117	116	117	118	118	118	111	120	116	118	119
C5	131	129	131	131	132	132	123	132	127	132	131
C6	117	115	117	117	116	116	110	118	113	117	116
C7	167	166	167	169	167	169	159	168	155	169	161
C8	64	62	63	63	63	63	53	61	64	63	63
C9	127	126	127	128	127	128	121	130	125	128	129
C10	126	125	127	127	127	128	120	128	111	127	114
C11	118	115	119	118	119	118	112	120	126	118	130
C12	157	154	156	155	155	154	145	152	152	155	158
C13	110	108	110	110	111	111	104	112	126	111	130
C14	125	122	125	124	126	125	118	126	111	125	114
C15	61	60	62	63	61	62	50	59	57	63	55

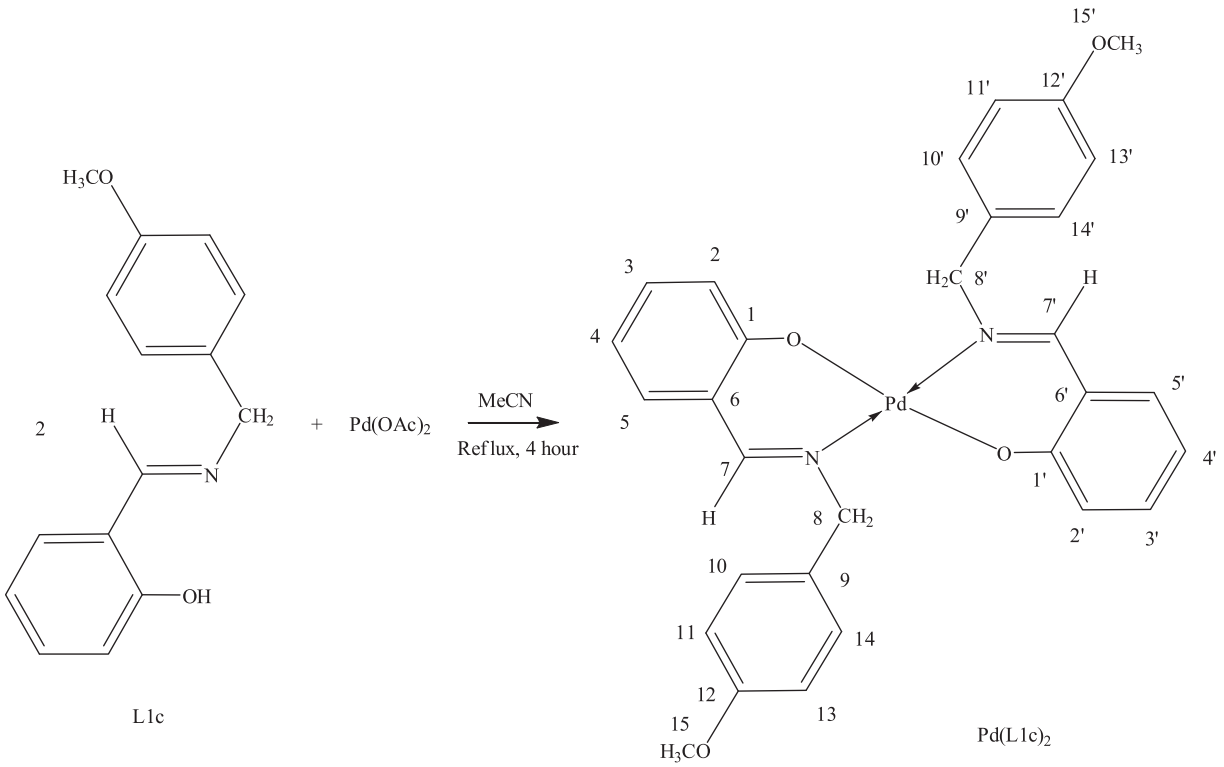

Scheme 2 Synthesis of $Pd(L1c)_2$ complex.

The predicted chemical shifts were obtained using the equation $\delta_{exp} = a\delta_{cal} + b$, where $\delta_{cal} = \delta_{iso}$.

The solvent effects were taken into account implicitly using polarisable continuum model (PCM) (Tomasi et al., 2005). In this model, the solute is embedded into a shape-adapted cavity surrounded by a dielectric continuum solvent, described by its dielectric constant (e.g., $\varepsilon_{CDCl3} = 4.7113$). The PCM has been reported to correctly model major solvent effects such as electrostatic effects of the medium providing no specific solute-solvent interactions such as hydrogen bond interactions, dipole-dipole interactions, or induced dipole-dipole interactions are considered (Jacquemin et al., 2009). Recently, Liu et al. reported that dipole-dipole interactions between coumarin and solvent molecules lead to large red shifts (Liu et al., 2013). For excited state energy calculations or time-dependent density functional theory (TD-DFT) calculations, solvent effects were considered by using IEF-PCM and state-specific solvation (SS-PCM) (Improta et al., 2006, 2007).

In a previous study, we tested both models to predict λ_{MAX} of terrein stereoisomers using different hybrid functionals, and the results proved that combination of SS-PCM formalism with M06-2X hybrid functional is reliable for excited-state predictions (Lumpi et al., 2013). All theoretical calculations were performed using Gaussian 09 package (Trucks et al., 2009).

3. Results and discussion

3.1. Ultraviolet-visible spectroscopy

The experimental and calculated $n \rightarrow \pi^*$ and $\pi \rightarrow \pi^*$ maximum absorption bands of L1c, $Ni(L1c)_2$ and $Pd(L1c)_2$ are reported in Tables 3 and 4, respectively.

The spectra were recorded in chloroform ($CHCl_3$) where the maximum absorption bands λ_{MAX} due to $n \rightarrow \pi^*$ for L1c, $Ni(L1c)_2$ and $Pd(L1c)_2$ were detected at 287, 389 and 399 nm respectively. Upon complexation, there is a significant increase in energy level difference between the non-bonding molecular orbital (n) with the pi anti-bonding molecular orbital (π^*). This shift to longer wavelengths with $\Delta\lambda$ of about 100 nm reflects a large bathochromic shift or a red shift caused by the change in the electronic environment of the ligand as the result of chelation with Ni(II) and Pd(II).

The λ_{MAX} for $\pi \rightarrow \pi^*$ transition for L1c, $Ni(L1c)_2$ and $Pd(L1c)_2$ were observed at 230, 234 and 246 nm, respectively. There is a slight increase of about 4–16 nm indicating a smaller degree of bathochromic shift where the energy level difference between π and π^* molecular orbitals became only slightly bigger upon complexation with Ni(II) and Pd(II). Fixing the energy level of the π^* orbital arbitrarily, the experimental values indicated that both the n and π orbitals became stabilised to lower energy levels upon complexation with n experiencing a bigger degree of stabilisation than π.

The calculated λ_{MAX} values were obtained in gas and solvent media using polarisable continuum model (PCM). For solvated model, the integral equation formalism (IEF-PCM) and surface and simulation (SS-PCM) formalism were applied. The predictions were carried out using B3LYP, B3P86, CAM-B3LY, M06-2X and PBE0 hybrid functionals. The comparison of the experimental and calculated values is discussed below.

3.1.1. $n \rightarrow \pi^*$ absorption band

Calculated $n \rightarrow \pi^*$ absorption bands for L1c, $Ni(L1c)_2$ and $Pd(L1c)_2$ are reported in Table 3. The B3LYP, B3P86 and PBE0

Table 2 Predicted and experimental ^{1}H and ^{13}C chemical shifts of $Pd(L1c)_2$ calculated at different levels and phases.

	B3LYP		B3P86		CAM-B3LYP		M06-2X		PBE0		Exp.
	Gas	IEF-PCM	Gas	IEF-PCM	Gas	IEF-PCM	Gas	IEF-PCM	Gas	IEF- PCM	
^{1}H NMR											
H2	6.8	6.8	6.8	6.9	6.8	6.9	6.9	7.0	6.8	6.9	6.6
H3	7.0	7.1	7.0	7.2	7.0	7.2	7.0	7.2	7.0	7.2	7.2
H4	6.5	6.6	6.5	6.8	6.5	6.7	6.5	6.8	6.5	6.8	7.2
H5	6.6	6.8	6.6	7.0	6.6	7.0	6.7	7.0	6.6	7.0	7.4
H7	7.6	7.7	7.5	7.7	7.6	7.7	7.5	7.6	7.5	7.7	7.7
H8	6.3	6.1	6.4	4.6	6.2	4.6	5.8	4.6	6.4	4.6	5.0
H10	6.8	7.0	6.8	7.1	6.8	7.1	6.9	7.1	6.8	7.1	7.4
H11	6.9	6.8	6.9	7.0	6.9	6.9	6.9	7.0	6.9	7.0	6.6
H13	6.3	6.5	6.3	6.6	6.3	6.6	6.5	6.7	6.3	6.6	6.6
H14	7.9	7.7	7.9	7.7	8.0	7.8	8.1	7.8	7.9	7.7	7.4
H15	4.0	3.8	4.0	4.4	4.0	4.5	4.0	4.4	4.0	4.4	3.9
^{13}C NMR											
C1	164	163	159	162	162	162	160	160	162	162	163
C2	125	125	159	125	126	125	128	128	126	125	163
C3	135	135	120	136	136	136	136	136	136	136	120
C4	119	119	133	119	119	119	120	120	119	119	135
C5	137	138	129	138	138	138	137	138	137	138	130
C6	122	122	133	122	120	120	122	124	121	122	134
C7	165	165	155	166	167	167	167	166	166	166	159
C8	69	68	64	68	69	69	67	67	68	67	59
C9	134	134	128	134	133	133	135	135	133	134	129
C10	131	131	114	132	131	132	132	132	131	132	114
C11	120	120	130	120	121	120	122	122	121	120	131
C12	159	159	154	158	157	156	155	155	158	158	158
C13	114	115	130	115	115	115	116	116	115	115	131
C14	134	134	114	134	135	134	135	135	135	134	114
C15	66	67	61	67	66	67	63	62	66	67	55

hybrid functionals failed to reproduce the experimental $n \rightarrow \pi^*$ absorption band for L1c. They underestimate the experimental value by 40, 40 and 32 nm, respectively. In IEF-PCM and SS-PCM formalisms, the variations were reduced to 36, 37, 30 nm, and 23, 24 and 17 nm, respectively. However, the calculated $n \rightarrow \pi^*$ absorption bands for L1c by using M06-2X and CAM-B3LYP hybrid functionals are comparable with the experimental values. The M06-2X hybrid functional gave better reproduction than CAM-B3LYP. Indeed, by using M06-2X (CAM-B3LYP) the variation to the experimental value in gas, IEF-PCM and SS-PCM is quite small of 2 (8), 1 (5) and 3 (2) nm, respectively.

In agreement with the experimental observation, a large bathochromic effect upon complexation *i.e.* shifting to significantly longer wavelengths was observed in all the calculated λ_{MAX}. This red shift can be explained by the stabilisation of HOMO orbitals. For instance, by using B3LYP hybrid functional, HOMO orbital was stabilised by 0.38 and 0.18 eV in IEF-PCM and SS-PCM, respectively. However, LUMO orbital was only slightly stabilised in IEF-PCM and SS-PCM, with relative energies of 0.08 and 0.07 eV, respectively (Fig. 1). As can be seen from HOMO and LUMO orbitals delocalisation in Fig. 1, HOMO-LUMO electronic transition induces a charge transfer from methoxybenzyl to salicyl moiety in L1c.

In a previous study (Anouar et al., 2012), we tested several hybrid functionals and basis sets to predict λ_{MAX} of a series of polyphenols; we showed that B3LYP and B3P86 are the most reliable for reproducing the maximum absorption bands. In another study, Jacquemin et al. (2004) showed that PBE0 and B3LYP were most suitable to reproduce λ_{MAX} of a series of anthraquinones. In fact, the reproducibility of λ_{MAX} depends mainly on the basic skeleton of the studied compounds, which explains the results obtained here. Recently, in an unreported study, we tested different hybrid functionals to predict λ_{MAX} of terrein stereoisomers; the results showed that the best reproductions were obtained using M06-2X hybrid functional and SS-PCM formalism.

3.1.2. $\pi \rightarrow \pi^*$ absorption band

The experimental absorption at 230 nm in UV–vis spectrum of L1c ligand corresponds to $\pi \rightarrow \pi^*$ electronic transition (Table 4) between HOMO-3 (or HOMO-2) and LUMO orbitals. In gas phase, this absorption band was well reproduced by using M06-2X and CAM-B3LYP hybrid functionals with standard deviations of 5 and 8 nm, respectively (Fig. 2).

On the contrary, the B3LYP, B3P86 and PBE0 hybrid functionals failed in reproduction of $\pi \rightarrow \pi^*$ with standard deviations of 25, 22 and 16 nm, respectively. In IEF-PCM, a bathochromic shift of 1–4 nm for $\pi \rightarrow \pi^*$ was obtained by using different tested hybrid functionals. In the SS-PCM formalism, a bathochromic shift of 1–6 nm was obtained using different hybrid functionals with regard to IEF-PCM model. In summary, for both electronic transitions $n \rightarrow \pi^*$ and $\pi \rightarrow \pi^*$ the best reproductions were obtained using M06-2X and CAM-B3LYP hybrid functionals in gas, IEF-PCM and SS-PCM.

Table 3 λ_{MAX} (nm), E_{MAX} (eV), f of $n \rightarrow \pi^*$ transitions of L1c and its complexes $Ni(L1c)_2$ and $Pd(L1c)_2$ calculated using B3LYP, PBE0, CAM-B3LYP, M06-2X and PBE0 hybrid functionals in gas, IEF-PCM and SS-PCM.

	Gas			IEF-PCM			SS-PCM			Exp.	
	λ_{MAX}	E_{MAX}	f	λ_{MAX}	E_{MAX}	f	λ_{MAX}	E_{MAX}	f	λ_{MAX}	E_{MAX}
B3LYP											
L1c	327	3.80	0.09	323	3.84	0.11	310	4.00	0.08	287	4.33
$Ni(L1c)_2$	404	3.07	0.07	400	3.10	0.08	397	3.12	0.06	389	3.20
$Pd(L1c)_2$	419	2.96	0.04	416	2.98	0.08	412	3.01	0.06	399	3.12
B3P86											
L1c	327	3.79	0.09	324	3.83	0.10	311	3.99	0.06	287	4.33
$Ni(L1c)_2$	403	3.08	0.06	401	3.09	0.07	398	3.11	0.06	389	3.20
$Pd(L1c)_2$	419	2.96	0.06	416	2.98	0.08	412	3.01	0.06	399	3.12
CAM-B3LYP											
L1c	295	4.21	0.14	292	4.25	0.18	289	4.29	0.13	287	4.33
$Ni(L1c)_2$	332	3.73	0.23	332	3.73	0.27	327	4.40	0.21	389	3.20
$Pd(L1c)_2$	344	3.60	0.18	344	3.61	0.23	339	3.66	0.17	399	3.12
M06-X2											
L1c	289	4.29	0.14	286	4.33	0.18	284	4.37	0.14	287	4.33
$Ni(L1c)_2$	314	3.94	0.30	316	3.92	0.35				389	3.20
$Pd(L1c)_2$	331	3.74	0.22	332	3.74	0.24	327	3.79	0.18	399	3.12
PBE0											
L1c	319	3.88	0.07	317	3.92	0.11	304	4.08	0.11	287	4.33
$Ni(L1c)_2$	379	3.27	0.08	378	3.28	0.11	374	3.31	0.08	389	3.20
$Pd(L1c)_2$	397	3.12	0.08	395	3.14	0.11	391	3.18	0.08	399	3.12

Table 4 λ_{MAX} (nm), E_{MAX} (eV), f of $\pi \rightarrow \pi^*$ transitions of L1c and its complexes $Ni(L1c)_2$ and $Pd(L1c)_2$ calculated using B3LYP, PBE0, CAM-B3LYP, M06-2X and PBE0 hybrid functionals in gas, IEF-PCM and SS-PCM.

	Gas			IEF-PCM			SS-PCM			Exp.	
	λ_{MAX}	E_{MAX}	f	λ_{MAX}	E_{MAX}	f	λ_{MAX}	E_{MAX}	f	λ_{MAX}	E_{MAX}
B3LYP											
L1c	255	4.86	0.32	256	4.84	0.33	252	4.93	0.34	230	5.41
$Ni(L1c)_2$	297	4.18	0.16	262	4.73	0.31	297	4.18	0.09	234	5.31
$Pd(L1c)_2$	296	4.19	0.21	297	4.18	0.34	294	4.22	0.21	246	5.06
B3P86											
L1c	252	4.91	0.32	254	4.89	0.33	249	4.97	0.28	230	5.41
$Ni(L1c)_2$	302	4.11	0.05	259	4.78	0.20	298	4.16	0.07	234	5.31
$Pd(L1c)_2$	294	4.21	0.23	296	4.20	0.36	293	4.24	0.23	246	5.06
CAM-B3LYP											
L1c	238	5.21	0.30	240	5.18	0.38	238	5.21	0.31	230	5.41
$Ni(L1c)_2$	222	5.58	0.18	236	5.24	0.50	232	5.33	0.66	234	5.31
$Pd(L1c)_2$	229	5.43	0.83	232	5.34	0.83	227	5.46	0.75	246	5.06
M06-X2											
L1c	235	5.28	0.33	236	5.25	0.42	235	5.29	0.34	230	5.41
$Ni(L1c)_2$	217	5.70	1.23	221	5.61	1.47				234	5.31
$Pd(L1c)_2$	225	5.51	0.61	228	5.45	1.40	220	5.64	0.49	246	5.06
PBE0											
L1c	246	5.05	0.21	251	4.93	0.40	244	5.09	0.32	230	5.41
$Ni(L1c)_2$	280	4.42	0.14	261	4.74	0.12	280	4.43	0.13	234	5.31
$Pd(L1c)_2$	281	4.41	0.27	282	4.39	0.40	280	4.44	0.24	246	5.06

3.2. ^1H and ^{13}C NMR spectroscopy

The structure of the Schiff base L1c and its complexes Ni $(L1c)_2$ and $Pd(L1c)_2$ were elucidated via NMR. The ^1H and ^{13}C NMR spectra of the synthesised compounds were recorded in deuterated chloroform ($CDCl_3$) using TMS as internal standard. The experimental ^1H NMR spectrum of L1c Schiff base showed the presence of an iminic proton (HC═N─) at δ 8.4 (1H, s, H7), methylene protons (─CH_2─) at δ 4.8 (2H, s, H8), methoxy protons (Ar─OCH_3) at δ 3.8 (3H, s, H15),

phenolic proton at δ 13.5 (1H, s, H1) and multiplets of aromatic protons δ 6.3–7.3 (Table 1 and Table 1S). The predicted ^{1}H NMR chemical shifts were calculated using five hybrid functionals (Table 1) as mentioned in Section 2.3. The correlation coefficients of regression curves between the experimental and predicted ^{1}H NMR chemical shifts are reported in the Supplementary material (Table 3S). In the gas phase, the best correlation was obtained using B3LYP hybrid functional with a R^2 of 98.76% (Table 3S). However, the variation between the other hybrid functionals is varied from 0.16 to 2.177. Taking the solvent effects into consideration, the correlation curves are relatively improved compared with those in gas phase (Table 3S). For instance, using B3P86 a variation of 1.23% was obtained between R^2 in PCM and gas phases. The complexation of L1c with Pd(II) induces the disappearance of phenolic proton at 13.5 ppm, due to its deprotonation, and the related oxygen involved in an ionic bond with central Pd(II). The rest of the ^{1}H NMR chemical shifts were slightly affected by the complexation. For instance, small downfield and upfield shifts were observed for methylene —CH_2— proton (by 0.2 ppm) and olefinic proton (by 0.7 ppm), respectively. The predicted ^{1}H NMR chemical shifts for Pd(L1c)$_2$ obtained using the tested hybrid functionals are shown in Table 2. Likewise, theoretical calculations showed downfield and upfield shifts of ^{1}H NMR chemical shifts in the complexes. The correlation coefficients of regression curves between the experimental and the predicted ^{1}H NMR chemical shifts for Pd(L1c)$_2$ complex are reported in the Supplementary material (Table 4S). In PCM, except B3LYP, all tested hybrid functionals could reproduce ^{1}H NMR chemical shifts with an R^2 of 90% (Table 4S).

The ^{13}C NMR spectrum of L1c Schiff base displayed fifteen carbon signals: one methoxy (—OCH_3), one methylene bridge (—CH_2—), nine methine (—CH—) and four quaternary carbons (Scheme 1 and Table 3). The ^{13}C NMR chemical shifts (with respect to TMS) were calculated using five tested hybrid functionals in gas and solvent by using IEF-PCM formalism (Tables 1 and S1). As can be seen from the correlation coefficients obtained between the experimental and the predicted ^{13}C NMR chemical shifts (Table 3S), all the tested hybrid functionals lead to similar results with an R^2 of 93 % in gas and solvent models. Similarly, the complexation of L1c induced downfield and upfield shifts of some ^{13}C NMR chemical shifts. However, these can be considered negligible, as the variation between ^{13}C NMR chemical shift of L1c and Pd(L1c)$_2$ was too small, between 1 and 4 ppm. In the complexes, the best correlation between experimental and predicted ^{13}C NMR chemical shifts was obtained using M06-2X hybrid functional, with an R^2 of 78% (Table 4S).

In summary, the correlation curves (or correlation coefficients) obtained with ^{1}H NMR were better than those with ^{13}C NMR, probably due to the sensitivity of ^{1}H compared to ^{13}C, which has low isotropic abundance. Theoretically, the predicted ^{13}C NMR chemical shifts were less independent of the choice of methodology (*i.e.,* similar R^2 obtained with different hybrid functionals). On the other hand, the predicted ^{1}H NMR chemical shifts were more dependent on the skeleton form of the ligand or complex, and to the choice of methodology. For instance, in L1c, the best correlation was obtained using B3LYP hybrid functional, while in Pd(L1c)$_2$, the best correlations were obtained using M06-2X, B3P86 and PBE0 hybrid functionals (Tables 3S and 4S).

3.3. Infrared spectroscopy

The experimental values of $\nu_{C=N}$ (C=N) recorded a decrease of 12 and 25 cm^{-1} when L1c was complexed with Ni(II) and Pd(II), respectively (Table 5). Following the Planck's equation of $E = h\nu$, lowering the frequency indicates a weakening of the imine bond. This could be due to the inductive effect of the Lewis acid-base interaction between the ligand and the metal centre where a lone pair of electrons is donated by the imine N to the metal centre, forming an M—N dative covalent bond, reducing the electron density on the C=N. The opposite is observed to be true for ν_{C-O}. Upon complexation, the stretching frequency of C—O was shown to increase by 70 and 77 cm^{-1} for Ni(II) and Pd(II) complexes, respectively (Table 5). The M—O bond formed upon complexation is an ionic bond when the phenolic proton is replaced by the metal causing the C—O bond to become stronger with the octet completing transfer of an electron from M to O.

The calculated $\nu_{C=N}$ (C=N) stretching harmonic vibrational frequencies of L1c Schiff base and its complexes, Ni(L1c)$_2$ and Pd(L1c)$_2$, are also reported in Table 5.

The calculated vibrational frequencies were obtained using the tested hybrid functionals, and the obtained values were scaled by a factor of 0.9679 (Mendoza-Wilson and Glossman-Mitnik, 2005). For $\nu_{C=N}$, the theoretical reproduction was successful with a low variation of 6 and 9 cm^{-1} obtained using B3P86 and PBE0 hybrid functionals. For Pd(L1c)$_2$ complex, both B3LYP and B3P86 could well reproduce the experimental $\nu_{C=N}$ vibration, with variation of 4 and

Table 5 $\nu_{C=N}$ vibrational modes for L1c and its complexes Ni(L1c)$_2$ and Pd(L1c)$_2$ calculated using B3LYP, B3P86, CAM-B3LYP, M06-2X and PBE0 hybrid functionals in gas.

Hybrid functionals	Vibration mode (cm^{-1})								
	L1c			Ni(L1c)$_2$			Pd(L1c)$_2$		
	Cal	Scal	Exp	Cal	Scal	Exp	Cal	Scal	Exp
B3LYP	1660	1607	1630	1642	1589	1618	1654	1601	1605
B3P86	1678	1624	1630	1686	1632	1618	1666	1612	1605
CAM-B3LYP	1710	1655	1630	1715	1660	1618	1711	1656	1605
M06-2X	1728	1672	1630	1718	1663	1618	1711	1656	1605
PBE0	1694	1639	1630	1700	1646	1618	1678	1624	1605

Cal = Calculated; Scal = Scaled; Exp = Experimental.

Table 6 Crystallographic data collection parameters for $Ni(L1c)_2$ and $Pd(L1c)_2$.

Compound	$Ni(L1c)_2$	$Pd(L1c)_2$
Empirical formula	$C_{30}H_{28}N_2O_4Ni$	$C_{30}H_{28}N_2O_4Pd$
Formula weight	539.26	586.94
Temperature (K)	−173	273
Wavelength (Å)	0.7107	0.7107
Crystal system	Monoclinic	Monoclinic
Space group	P21/c	P21/c
Unit cell dimensions (Å)	a = 12.184(2); b = 5.673(10); c = 17.762(3)	a = 12.329(4); b = 5.647(19); c = 18.291(6)
β (°)	β = 95.682(10)	β = 96.658(6)
Volume ($Å^3$)	1221.92(4)	1264.90(7)
Z	4	2
Absorption coefficient (mm^{-1})	0.84	0.77
Crystal size (mm)	0.52 × 0.30 × 0.16	0.50 × 0.19 × 0.10
θ range (°)	1.7–32.7	1.7–28.4
Index ranges	$-18 \leqslant h \leqslant 17$ $-8 \leqslant k \leqslant 8$ $-26 \leqslant l \leqslant 26$	$-16 \leqslant h \leqslant 16$ $-7 \leqslant k \leqslant 7$ $-24 \leqslant l \leqslant 20$
F (000)	564	600
Goodness-of-fit on F2	1.091	1.072
Final R indices	$R1$ = 0.0308, w$R2$ = 0.0818	$R1$ = 0.0362, w$R2$ = 0.0802
R indices (all data)	$R1$ = 0.0385, w$R2$ = 0.0894	$R1$ = 0.0532, w$R2$ = 0.0865
CCDC no.	1,014,286	1,513,134

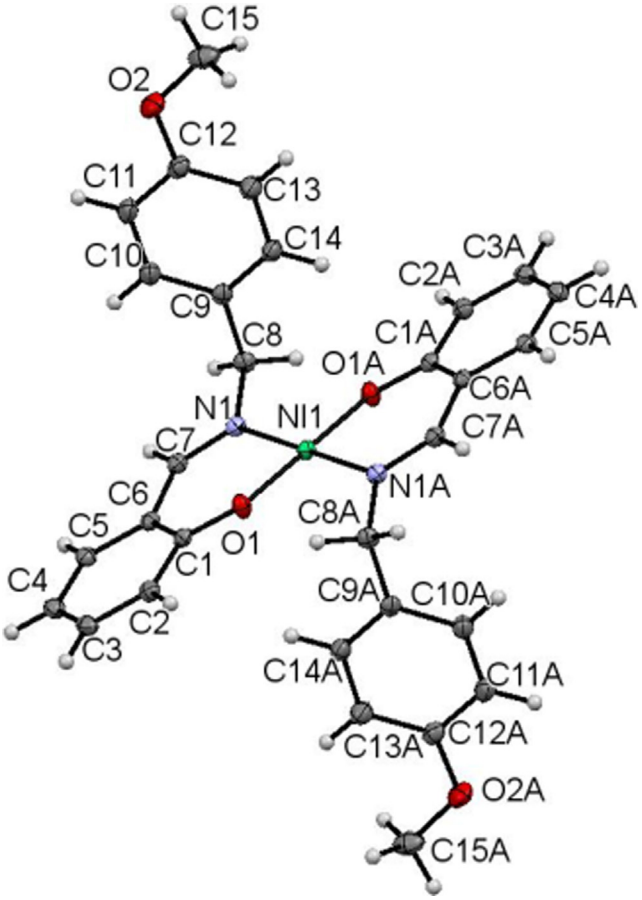

Figure 3 ORTEP diagram of $Ni(L1c)_2$ drawn at 50% probability ellipsoids.

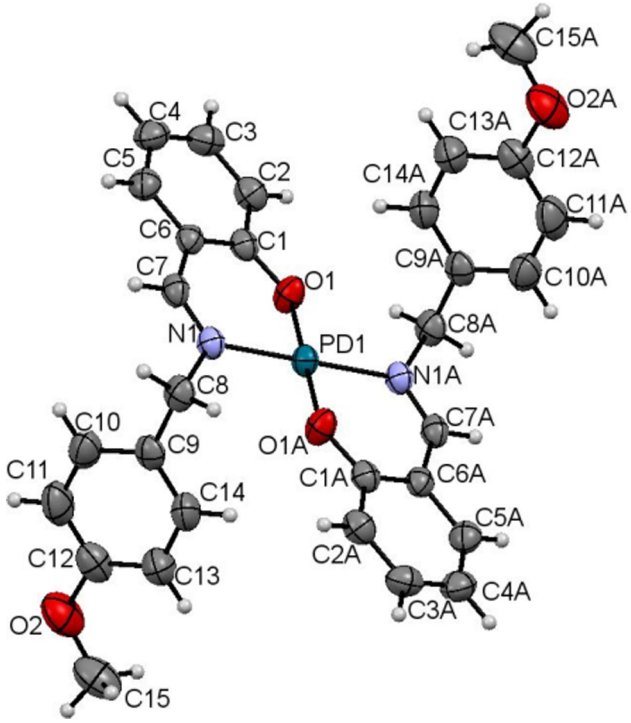

Figure 4 ORTEP diagram of $Pd(L1c)_2$ drawn at 50% probability ellipsoids.

7 cm^{-1}, respectively. However in $Ni(L1c)_2$, the reproduction of $\nu_{C=N}$ was less successful for all the tested hybrid functionals with variations ranging from 14 to 45 cm^{-1}. The complexation of L1c induces a bathochromic shift of ν_{C-O} (C—O) at 1248 cm^{-1} to 1325 and 1348 cm^{-1} for $Ni(L1c)_2$ and $Pd(L1c)_2$, respectively. However, the complexation effect on the vibration modes theoretically depends on the method chosen. The best correlation was obtained through B3P86 hybrid functional where the complexation of L1c with Pd induces a decrease of vibration by 12 cm^{-1}.

Table 7 Some important bond lengths (Å) and angles (°).

Bond length/angle	$Ni(L1c)_2$	$Pd(L1c)_2$
O1-C1	1.3085(14)	1.310(3)
N1-C7	1.297(16)	1.286(3)
N1-C8	1.486(15)	1.486(3)
M-O1	1.8410(9)	1.9481(19)
M-N1	1.9200(11)	2.1023(4)
N1-M-O1	87.69(4)	88.81(8)
N1-M-O1A	92.31(4)	91.91(8)

3.4. X-ray crystallography

Single crystals of $Ni(L1c)_2$ and $Pd(L1c)_2$ were subjected to X-ray crystallography investigation to determine their structures. The crystals were obtained by slow evaporation of chloroform solution at room temperature. Both complexes crystallised in monoclinic system with space group P21/c. The crystal system and refinement parameters for $Ni(L1c)_2$ and $Pd(L1c)_2$ are given in Table 6. The molecular structures of the complexes $Ni(L1c)_2$ and $Pd(L1c)_2$ with numbering scheme are shown in Figs. 3 and 4.

Both complexes are symmetrically generated at the metal centres. Each complex has two ligands coordinated to the metal via nitrogen and oxygen atoms in bidentate manner to form a distorted square planar environment. The bond angles about the central Ni1 atom of O1-Ni-N1 and O1A-Ni-N1A are 87.69(4) and 92.31(4), respectively. The bond angles about Pd1 are slightly less distorted as shown by the O1-Pd-N1 and O1A-Pd-N1A of 91.20(8) and 88.81(8)°, respectively.

The Ni1-N1, Ni1-O1, Pd1-N1 and Pd1-O1 lengths of 1.9191(11), 1.8407(9), 2.023(2) and *1*.984(2) Å, respectively are consistent with the normal metal-O and metal-N bond lengths observed in other similar nickel(II) complexes (Bahron et al., 2011) and Pd(II) complexes (Mohd Tajuddin et al., 2010; Adrian et al., 2008). Other bond lengths and angles in the coordinated ligand are in normal ranges. The O1-C1, N1-C7 and N1-C8 bond lengths in both complexes are comparable (Table 7) and in agreement with those reported in the analogous complexes (Adrian et al., 2008).

Overall, the complexes display an essentially planar bidentate metal /O1/N1/C1/C6/C7 6-membered ring coordination with maximum deviation of 0.152 and 0.149 Å for Ni1 and Pd1 atoms, respectively. The O2/(C8-C15) p-methoxybenzyl groups in both complexes are planar with maximum deviation of 0.074(2) Å for C15 atom from the least square plane in the nickel complex. In both complexes the two methoxybenzyl groups are facing in opposite direction almost perpendicular to the 6-membered bidentate ring with dihedral angle of 82.77(5) and 82.45(10)° in nickel and palladium complexes respectively.

Z-matrix coordinates of L1c, $Ni(L1c)_2$ and $Pd(L1c)_2$ were calculated within the five tested hybrid functionals in gas and PCM (Table 5S). Generally, good agreements were obtained between calculated structural and experimental X-ray parameters (Table 6S). In both phases, the standard errors between the experimental and calculated bond lengths of L1c and its complexes $Ni(L1c)_2$ and $Pd(L1c)_2$ obtained with different hybrid functionals were very negligible with variation less than 0.09 Å. In the case of bond angles, the standard errors vary from 1 to 5°. These low values explain the good correlations obtained for bond lengths and bond angles ($R^2 \geqslant 90°$). However, the torsion angle standard errors and correlation coefficient strongly depended on the form of Schiff base (free or coordinated to Ni and Pd). For the free Schiff base, all the torsion angles were well-reproduced (100%). However, for the complexes, the standard errors varied. For $Pd(L1c)_2$, the standard errors were less than 3°, while for $Ni(L1c)_2$ they were varied between 1° and 34°. The lowest standard errors were obtained with CAM-B3LYP, M06-2X. In summary, X-ray crystallography parameters were well-reproduced by different hybrid functionals.

3.5. Biological activity screening

Table 8 shows biological activity of L1c and its complexes against HCT116 and *E. coli*. The results reveal that the ligand L1c is more active as anticancer and antibacterial agents than its complexes. The ligand is about 17 times more potent in killing the HCT116 colorectal cancer cells than the complexes. Similarly, the ligand also showed a strong antibacterial activity against *E. coli* with inhibition zone of 19.33 mm, better than the positive control Gentamicin (15.50 mm). Surprisingly, the antibacterial activity disappeared when the ligand is complexed with nickel and palladium metals.

4. Conclusion

((*E*)-(4-methoxybenzylimino)methyl)phenol Schiff base, named L1c and its complexes $Ni(L1c)_2$ and $Pd(L1c)_2$, were successfully synthesised. The molecular structures of the synthesised compounds were confirmed by spectroscopic and X-ray techniques. The experimental data were compared to the calculated DFT and TD-DFT calculation results. For UV–vis reproduction, the results showed that CAM-B3LY and M06-2X are the most suitable. NMR chemical shift predictions showed that the ^{1}H NMR chemical shifts are strongly influenced by the tested hybrid functionals, whereas the ^{13}C chemical shift is less influenced. The reproduction of the IR vibrations modes was also dependent on the tested hybrid functionals. Finally, the entire tested hybrid functionals were successfully reproduced as experimental X-ray parameters. The influence of complexation of L1c is more empha-

Table 8 The biological activity test of L1c and its $Pd(L1c)_2$ and $Pd(L1c)_2$ complexes.

Compound	Empirical formula	Molecular weight (g/mol)	Colour	Anticancer activity against HCT116 (IC_{50}, μM)	Antibacterial activity against *E. coli* (Zone of inhibition, mm)
L1c	$C_{15}H_{15}NO_2$	241.29	Yellow	9.95 (active)	19.33 (active)
$Pd(L1c)_2$	$C_{30}H_{28}N_2O_4Pd$	586.97	Turmeric yellow	>170.37 (not active)	0.00 (not active)
$Ni(L1c)_2$	$C_{30}H_{28}N_2O_4Ni$	539.25	Green	>185.44 (not active)	0.00 (not active)
Positive control				5.76 5-FU	15.50 (Gentamicin)

sised in UV–vis and IR spectroscopy. However, in the case of NMR chemical shifts and X-ray parameter predictions, the complexation effects are negligible. The chelation of nickel and palladium to the ligand L1c reduced significantly the anticancer and antibacterial property against the tested cell and microbe.

Acknowledgement

The authors would like to acknowledge the Ministry of Higher Education of Malaysia for the research funding through Research Acculturation Grant Scheme (600-RMI/RAGS 5/3 (8/2015) and Universiti Teknologi MARA for the use of research facilities and Universiti Kebangsaan Malaysia Center for Research and Instrumentation Management (CRIM) for the chemical crystallography studies.

Appendix A. Supplementary material

Supplementary data associated with this article can be found, in the online version, at http://dx.doi.org/10.1016/j.arabjc.2016.11.005.

References

Abdul Ghani, A., Bahron, H., Harun, M.K., Kassim, K., 2014. Malay. J. Anal. Sci. 18, 507–513.
Adrian, R.A., Broker, G.A., Tiekink, E.R., Walmsley, J.A., 2008. Inorg. Chim. Acta 361, 1261–1266.
Alberto, M.E., De Simone, B.C., Mazzone, G., Quartarolo, A.D., Russo, N., 2014a. J. Chem. Theory Comput. 10, 4006–4013.
Alberto, M.E., Mazzone, G., Quartarolo, A.D., Sousa, F.F.R., Sicilia, E., Russo, N., 2014b. J. Comput. Chem. 35, 2107–2113.
Andersson, M., Uvdal, P., 2005. J. Chem. Phys. A 109, 2937–2941.
Anouar, E.H., Gierschner, J., Duroux, J.-L., Trouillas, P., 2012. Food Chem. 131, 79–89.
Bahron, H., Tajuddin, A.M., Ibrahim, W.N.W., Hemamalini, M., Fun, H.-K., 2011. Acta Crystallogr. E 67, m1010–m1011.
Bak, K., Hansen, A., Ruud, K., Helgaker, T., Olsen, J., Jørgensen, P., 1995. Theoret. Chim. Acta 90, 441–458.
Bauernschmitt, R., Ahlrichs, R., 1996. Chem. Phys. Lett. 256, 454–464.
Becke, A.D., 1993. J. Chem. Phys. 98, 5648–5652.
Casida, M.E., Jamorski, C., Casida, K.C., Salahub, D.R., 1998. J. Chem. Phys. 108, 4439–4449.
Cheeseman, J.R., Trucks, G.W., Keith, T.A., Frisch, M.J., 1996. J. Chem. Phys. 104, 5497–5509.
Chohan, Z.H., Pervez, H., Rauf, A., Khan, K.M., Maharvi, G.M., Supuran, C.T., 2004. J. Enzyme Inhib. Med. Chem. 19, 161–168.
Chohan, Z.H., Pervez, H., Rauf, A., Khan, K.M., Supuran, C.T., 2006. J. Enzyme Inhib. Med. Chem. 21, 193–201.
Chohan, Z.H., Arif, M., Shafiq, Z., Yaqub, M., Supuran, C.T., 2006. J. Enzyme Inhib. Med. Chem. 21, 95–103.
Cui, J., Zhang, M., Zhang, Y., 2010. Inorg. Chem. Commun. 13, 81–85.
Ebrahimipour, S.Y., Abaszadeh, M., Castro, J., Seifi, M., 2014. Polyhedron 79, 138–150.
Furche, F., Ahlrichs, R., 2002. J. Chem. Phys. 117, 7433–7447.
Furche, F., Ahlrichs, R., 2002. J. Chem. Phys. 117, 7433.
Gauss, J., 1992. Chem. Phys. Lett. 191, 614–620.
Gauss, J., 1993. J. Chem. Phys. 99, 3629–3643.
Gauss, J., 1995. Ber. Bunsen-Ges. 99, 1001–1008.
Guo, Z., Xing, R., Liu, S., Zhong, Z., Ji, X., Wang, L., Li, P., 2007. Carbohydr. Res. 342, 1329–1332.
Gupta, K., Sutar, A.K., 2008. Coord. Chem. Rev. 252, 1420–1450.
Improta, R., Barone, V., Scalmani, G., Frisch, M.J., 2006. J. Phys. Chem. 125, 054103.
Improta, R., Scalmani, G., Frisch, M.J., Barone, V., 2007. J. Phys. Chem. 127, 074504.
Jacquemin, D., Preat, J., Charlot, M., Wathelet, V., Andre, J.-M., Perpete, E.A., 2004. J. Chem. Phys. 121, 1736–1743.
Jacquemin, D., Preat, J., Wathelet, V., Fontaine, M., Perpète, E.A., 2006. J. Am. Chem. Soc. 128, 2072–2083.
Jacquemin, D., Perpete, E.A., Scuseria, G.E., Ciofini, I., Adamo, C., 2007. J. Chem. Theory Comput. 4, 123–135.
Jacquemin, D., Wathelet, V., Preat, J., Perpète, E.A., 2007. Spectrochim. Acta Mol. Biomol. Spectrosc. 67, 334–341.
Jacquemin, D., Wathelet, V., Perpete, E.A., Adamo, C., 2009. J. Chem. Theory Comput. 5, 2420–2435.
Ju, H., Kai, Z.-P., Li, Y., 2008. Corros. Sci. 50, 865–871.
Kabeer, A.S., Baseer, M., Mote, N., 2001. Asian J. Chem. 13, 496–500.
Khan, K.M., Ahmad, A., Ambreen, N., Amyn, A., Perveen, S., Khan, S.A., Choudhary, M.I., 2009. Lett. Drug Des. Discov. 6, 363–373.
Li, S., Chen, S., Lei, S., Ma, H., Yu, R., Liu, D., 1999. Corros. Sci. 41, 1273–1287.
Liu, X., Cole, J.M., Low, K.S., 2013. J. Phys. Chem. C 117, 14731–14741.
Lumpi, D., Horkel, E., Plasser, F., Lischka, H., Fröhlich, J., 2013. ChemPhysChem 14, 1016–1024.
Mazzone, G., Russo, N., Sicilia, E., 2013. Can. J. Chem. 91, 902–906.
Mendoza-Wilson, A.M., Glossman-Mitnik, D., 2005. J. Mol. Struct-Theochem. 716, 67–72.
Mohammed Khan, K., Taha, M., Naz, F., Siddiqui, S., Ali, S., Rahim, F., Perveen, S., Iqbal Choudhary, M., 2012a. Med. Chem. 8, 705–710.
Mohammed Khan, K., Shah, Z., Uddin Ahmad, V., Khan, M., Taha, M., Rahim, F., Ali, S., Ambreen, N., Perveen, S., Iqbal Choudhary, M., 2012b. Med. Chem. 8, 452–461.
Mohd Tajuddin, A., Bahron, H., Wan Ibrahim, W., Yamin, B.M., 2010. Acta Crystallogr. E 66. m1100–m1100.
Negm, N.A., Zaki, M.F., 2008. Colloids Surface A 322, 97–102.
Pattanayak, P., Pratihar, J.L., Patra, D., Lin, C.-H., Paul, S., Chakraborty, K., 2013. Polyhedron 51, 275–282.
Quartarolo, A.D., Russo, N., 2011. J. Chem. Theory Comput. 7, 1073–1081.
Ramakrishna, D., Bhat, B.R., Karvembu, R., 2010. Catal. Commun. 11, 498–501.
Ramos Sousa, F.F., Quartarolo, A.D., Sicilia, E., Russo, N., 2012. J. Phys. Chem. B 116, 10816–10823.
Sauri, A., Kassim, K., Bahron, H., Yahya, M., Harun, M., 2013. Mater. Res. Innov. 13, 4.
Scalmani, G., Frisch, M.J., Mennucci, B., Tomasi, J., Cammi, R., Barone, V., 2006. J. Chem. Phys. 124, 094107.
Schiff, H., 1864. Just. Lieb. Ann. Chem. 131, 118–119.
Taha, M., Baharudin, M.S., Ismail, N.H., Khan, K.M., Jaafar, F.M., Siddiqui, S., Iqbal Choudhary, M., 2013. Bioorg. Med. Chem. Lett. 23, 3463–3466.
Tarafder, M., Kasbollah, A., Saravanan, N., Crouse, K.A., Ali, A.M., 2002. J. Biochem. Mol. Biol. Biophys. 6, 85–91.
Tomasi, J., Mennucci, B., Cammi, R., 2005. Chem. Rev. 105, 2999–3093.
Trucks, G.W., Frisch, M.J., Schlegel, H.B., Scuseria, G.E., Robb, M. A., Cheeseman, J.R., Scalmani, G., Barone, V., Mennucci, B., Petersson, G.A., Nakatsuji, H., Caricato, M., Li, X., Hratchian, H. P., Izmaylov, A.F., Bloino, J., Zheng, G., Sonnenberg, J.L., Hada, M., Ehara, M., Toyota, K., Fukuda, R., Hasegawa, J., Ishida, M., Nakajima, T., Honda, Y., Kitao, O., Nakai, H., Vreven, T., Montgomery Jr, J.A., Peralta, J.E., Ogliaro, F., Bearpark, M., Heyd, J.J., Brothers, E., Kudin, K.N., Staroverov, V.N., Kobayashi, R., Normand, J., Raghavachari, K., Rendell, A., Burant, J.C., Iyengar, S.S., Tomasi, J., Cossi, M., Rega, N., Millam, J.M., Klene, M., Knox, J.E., Cross, J.B., Bakken, V., Adamo, C., Jaramillo, J., Gomperts, R., Stratmann, R.E., Yazyev, O., Austin, A.J., Cammi,

R., Pomelli, C., Ochterski, J.W., Martin, R.L., Morokuma, K., Zakrzewski, V.G., Voth, G.A., Salvador, P., Dannenberg, J.J., Dapprich, S., Daniels, A.D., Farkas, O., Foresman, J.B., Ortiz, J. V., Cioslowski, J., Fox, D.J., 2012. Gaussian 09, Revision A.02.

Vázquez-Vuelvas, O.F., Hernández-Madrigal, J.V., Gaviño, R., Tlenkopatchev, M.A., Morales-Morales, D., Germán-Acacio, J. M., Gomez-Sandoval, Z., Garcias-Morales, C., Ariza-Castolo, A., Pineda-Contreras, A., 2011. J. Mol. Struct. 987, 106–118.

Wolinski, K., Hinton, J.F., Pulay, P., 1990. J. Am. Chem. Soc. 112, 8251–8260.

Woodford, J.N., 2005. Chem. Phys. Lett. 410, 182–187.

Yurt, A., Ulutas, S., Dal, H., 2006. Appl. Surf. Sci. 253, 919–925.

Zainoldin, Z., Harun, M.K., Bahron, H., Kassim, K., 2012. Electrodeposition of salicylideneaniline and its corrosion behavior. In: Advanced Materials Research. Trans Tech Publ, pp. 385–389.